

Effect of hydrogen plasma implantation on the micro-structure and magnetic properties of hcp-$Co_{80}{}^{57}Fe_4Ir_{16}$ thin films

Hui Wang(王辉), Meng Wu(吴猛), Haiping Zhou(周海平), Bo Zhang(张博), Shixin Hu(胡世欣), Tianyong Ma(马天勇), Zhiwei Li(李志伟), Liang Qiao(乔亮), Tao Wang(王涛), Fashen Li(李发伸)

Citation: Chin. Phys. B, 2021, 30 (**5**): 057505. DOI: 10.1088/1674-1056/abe0c3
Journal homepage: http://cpb.iphy.ac.cn; http://iopscience.iop.org/cpb

What follows is a list of articles you may be interested in

Experiments and SPICE simulations of double MgO-based perpendicular magnetic tunnel junction

Qiuyang Li(李求洋), Penghe Zhang(张蓬鹤), Haotian Li(李浩天), Lina Chen(陈丽娜), Kaiyuan Zhou(周恺元), Chunjie Yan(晏春杰), Liyuan Li(李丽媛), Yongbing Xu(徐永兵), Weixin Zhang(张卫欣), Bo Liu(刘波), Hao Meng(孟浩), Ronghua Liu(刘荣华), and Youwei Du(都有为)

Chin. Phys. B, 2021, 30 (**4**): 047504. DOI: 10.1088/1674-1056/abdea2

Influence of additives on the magnetic damping constant of CoIr soft magnetic thin films with negative magnetocrystalline anisotropy

Tianyong Ma(马天勇), Zhi Luo(罗智), Zhiwei Li(李志伟), Liang Qiao(乔亮), Tao Wang(王涛), Fashen Li(李发伸)

Chin. Phys. B, 2019, 28 (**5**): 057505. DOI: 10.1088/1674-1056/28/5/057505

Computational study of inverse ferrite spinels

A EL Maazouzi, R Masrour, A Jabar, M Hamedoun

Chin. Phys. B, 2019, 28 (**5**): 057504. DOI: 10.1088/1674-1056/28/5/057504

Phase diagrams and magnetic properties of the mixed spin-1 and spin-3/2 Ising ferromagnetic thin film:Monte Carlo treatment

B Boughazi, M Boughrara, M Kerouad

Chin. Phys. B, 2019, 28 (**2**): 027501. DOI: 10.1088/1674-1056/28/2/027501

Magnetic properties of $L1_0$ FePt thin film influenced byrecoverable strains stemmed from the polarization of $Pb(Mg_{1/3}Nb_{2/3})O_3$-$PbTiO_3$ substrate

Li-Wang Liu(刘立旺), Cheng-Chao Hu(胡成超), Ye-Chuan Xu(徐野川), Hou-Bing Huang(黄厚兵), Jiang-Wei Cao(曹江伟), Linyun Liang(梁林云), Wei-Feng Rao(饶伟锋)

Chin. Phys. B, 2018, 27 (**7**): 077503. DOI: 10.1088/1674-1056/27/7/077503

Effect of hydrogen plasma implantation on the micro-structure and magnetic properties of hcp-$Co_{80}{}^{57}Fe_4Ir_{16}$ thin films*

Hui Wang(王辉)[1], Meng Wu(吴猛)[2], Haiping Zhou(周海平)[3], Bo Zhang(张博)[1], Shixin Hu(胡世欣)[1], Tianyong Ma(马天勇)[4], Zhiwei Li(李志伟)[1,†], Liang Qiao(乔亮)[1], Tao Wang(王涛)[1,‡], and Fashen Li(李发伸)[1]

[1] *Key Laboratory for Magnetism and Magnetic Materials of the Ministry of Education, Key Laboratory for Special Functional Materials and Structure Design of the Ministry of Education, Lanzhou University, Lanzhou* 730000, *China*

[2] *Department of Physics, Xiamen University, Xiamen* 361005, *China*

[3] *School of Materials and Energy, University of Electronic Science and Technology of China, Chengdu* 611731, *China*

[4] *School of Electrical and Information Engineering, North Minzu University, Yinchuan* 750021, *China*

(Received 25 November 2020; revised manuscript received 24 January 2021; accepted manuscript online 28 January 2021)

We present detailed investigations of structural and static/dynamic magnetic properties of hydrogenated hcp-$Co_{80}{}^{57}Fe_4Ir_{16}$ soft magnetic thin films. Two different kinds of defects, *i.e.*, destructive and non-destructive, were demonstrated by controlling the negative bias voltage of the hydrogenation process. Our results show that the structure and magnetic properties of our sample can be tuned by the density of the induced defects. These results provide better understanding of the hydrogenation effect and thus can be used in the future for materials processing to meet the requirements of different devices.

Keywords: soft magnetic thin film, hydrogen plasma implantation, Mössbauer spectroscopy

PACS: 75.70.–i, 75.50.Ss **DOI:** 10.1088/1674-1056/abe0c3

1. Introduction

With the increasing speed of information processing and transmission frequency, the performance of materials used in various devices working at giga hertz frequencies is undergoing more and more severe tests. Soft magnetic thin films (SMTFs) with adjustable high-frequency magnetic properties are highly desirable due to their wide range of applications, such as film inductors,[1,2] micro-transformers,[3] and microwave noise filters,[4,5] *etc*. Various methods have been proposed for the development of these SMTFs, such as chemical substitution,[6–10] high temperature and high magnetic field annealing,[11–15] crystal texture,[16] and hydrogen ion implantation,[17–20] *etc*. Among these methods, hydrogen implantation has been shown to be a powerful platform to tailor the physical properties of both transition metal oxides and various kinds of metal alloys.

Different hydrogenation methods have been reported in literatures, *e.g.*, the Pt-catalyst-assisted hydrogen spillover method,[17] the electrolyte gating methods,[18,19] the high energy hydrogen ion irradiation method,[21] and low-energy hydrogen ion plasma implantation method.[20] It was shown that not only the physical properties can be tuned by these hydrogenation processes but also emergent novel electronic phases can be discovered. Lu *et al.* reported a new $HSrCoO_{2.5}$ insulating ferromagnetic phase emerged from electric field controlled hydrogenation of the strontium cobaltite thin film by electrolyte gating method.[22] Jo *et al.* have shown that the metal–insulating phase can be greatly changed through the hydrogen spillover method.[18] Hydrogenation was also widely used in the preparation of various magnetic materials due to its active properties. Ho *et al*. have shown that the saturation magnetization (M_s) can be greatly improved by hydrogenation of the amorphous FeSiBC, FeNiMoSiB, and CoFeCrSiB magnetic materials.[23] However, the hydrogenation process would degrade other soft magnetic properties by making these materials highly brittle and with an increased coercive field (H_c). Zamani *et al*. have found that the Curie temperature of FeZr magnetic thin films can be increased by hydrogen implantation.[24] Pourarian *et al*. have explored the effect of hydrogen implantation on the rare earth-transition metal systems.[25] The defects and impurity segregation effect of the SiGe, SiC materials by hydrogen irradiation have also attracted a lot of attention.[26–28] Despite enormous effort has been put into the investigation of these defects and/or segregated phases, it is still puzzling us how these defects affect the properties of the studied mother systems.

In the present work, we report the investigation of the hydrogenation effect on the well-studied Co–Ir alloy system,[16,29–31] which exhibits negative magnetocrystalline anisotropy with proper Co/Ir ratios in the favor for high-frequency applications,[16] by using an elaborated low-energy hydrogen plasma implantation method.[20] This method has

*Project supported by the National Natural Science Foundation of China (Grant Nos. 11704167, 11704317, and 11574122).

†Corresponding author. E-mail: zweili@lzu.edu.cn

‡Corresponding author. E-mail: wtao@lzu.edu.cn

© 2021 Chinese Physical Society and IOP Publishing Ltd

been shown to be less time-consuming, does not need chemical reaction or high energy ion irradiation environments, and is less destructive to the samples under study. By tuning the negative bias voltage of the hydrogenation process, two groups of hydrogenated samples have been identified and studied in detail. Our results demonstrate that two different kinds of hydrogenation induced defects can be introduced into the studied Co–Ir alloy system by using low and high energy protons. The effect of these defects on the structure and magnetic properties of our films have been studied in detail.

2. Experiment

As reported in our earlier work,[16] the studied films adopt the hcp-type structure (see Fig. 1(a)) grown with its c direction normal to the film surface and with a c-lattice constant of 4.1186 Å. The pristine films were prepared by perpendicular DC magnetron sputtering technique with a layered structure of substrate/Ti/Au/$Co_{80}{}^{57}Fe_4Ir_{16}$. Substrate was taken from commercial Si wafer with (100) surface orientation. Before deposition of the $Co_{80}{}^{57}Fe_4Ir_{16}$ layer, an amorphous layer of Ti (7 nm) and a seed layer of Au (34 nm) were deposited in order to induce the c-axis orientation of the hcp-$Co_{80}{}^{57}Fe_4Ir_{16}$ magnetic layer. The base pressure of the deposition chamber was better than 5×10^{-5} Pa. For the deposition of the seed layer, pure Ar gas was used as the sputtering atmosphere with a pressure of 0.25 Pa. Several pieces of Ir and ^{57}Fe placed symmetrically on top of the Co target were used for the deposition of the $Co_{80}{}^{57}Fe_4Ir_{16}$ layer. The Ar pressure was set to 0.3 Pa and a substrate temperature of 350 °C was used for better crystallinity. The ^{57}Fe was used as Mössbauer probe for our Mössbauer spectroscopy measurements.

The hydrogenation process was done with a home-made plasma facility.[20] An adopted low-frequency inductively coupled plasma system was used to generate the required high density hydrogen plasma. A negative DC bias in the range of −60 V to −250 V was applied to control the built-in electric field of the plasma, leading to a dominant accumulation of protons near our film surface as shown in Fig. 1(b). The whole process was conducted at a vacuum pressure of 5 Pa and at a base temperature of 400 °C.

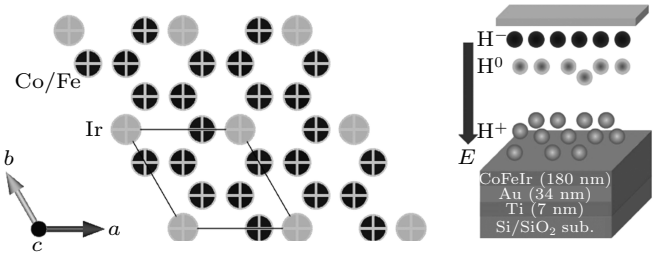


Fig. 1. Schematic views of (a) hcp-$Co_{80}{}^{57}Fe_4Ir_{16}$ crystal structure and (b) the hydrogen plasma implantation process with an applied DC bias to provide the implanted protons near the film surface.

All the films were characterized at room temperature and stored under vacuum except for the measurements procedure. Chemical compostion of these films have been characterized by using energy dispersive spectrometer (EDS) equipped within a scanning electron microscope (SEM). Microstructure and grain morphology were measured using transmission electron microscope (TEM). Crystal structure of our films were characterized by x-ray diffraction (XRD) with Cu $K_{\alpha 1}$ radiation. Static magnetic properties were measured with a vibrating sample magnetometer (VSM). The microwave permeability measurements were done with a vector network analyzer (VNA) using the shorted microstrip method. ^{57}Fe conversion electron Mössbauer spectroscopy (CEMS) measurements were performed with a conventional Mössbauer spectrometer (Wissel, Germany) working at constant acceleration mode. A 25-mCi γ-ray source of ^{57}Co embedded in Rhodium matrix was used. α-Fe foil was used to calibrate the drive velocity of the spectrometer and all isomer shifts are reported relative to that of the α-Fe.

3. Results and discussion

For the hydrogenation procedure, we have tried different conditions and found out that the most important one is the negative bias voltage which should be the parameter that controls the energy of the injected protons. Therefore, by controlling the negative bias voltage in the range of −60 V to −250 V while keeping other parameters similar, we have identified two groups of hydrogenated samples marked with sample 1 (−60 V)/sample 2 (−80 V) as group 1 (lower bias) and with sample 3 (−160 V)/sample 4 (−250 V) as group 2 (higher bias). The XRD patterns of the pristine sample together with that of the hydrogenated samples were shown in Fig. 2(a). As can be seen, the diffraction peaks can be identified, from lower to higher two theta angles, as (111) peak of the Au-seed layer, (002) peak of the hcp-$Co_{80}{}^{57}Fe_4Ir_{16}$ layer and (400) peaks of the Si substrate, respectively. No other impurity peaks can be seen for all these samples. From Fig. 2(a), one can see that the (002) peak shifts a little leftwards for the samples in group 1, suggesting an expansion of the c-axis lattice constant. On the other hand, the (002) peak shifts rightwards for the samples in group 2, indicating a shrinkage of the c-axis lattice parameter. The extracted c-axis lattice parameters for these samples were plotted in Fig. 2(b) with the value of the pristine sample marked as a horizontal dash-line. The full width at half maximum (FWHM) values of the (002) peak were also plotted. Clearly, the FWHM values for the samples in group 1 are similar to that of the pristine sample while the values for the samples in group 2 are much larger indicating more disorders induced by the hydrogenation process for the group-2 samples. One should notice that this is different for the Au-seed layer where one can see in Fig. 2(a) that all the (111) peaks shift

towards higher angles indicating shrinkage of the unit cell for all these bias voltages.

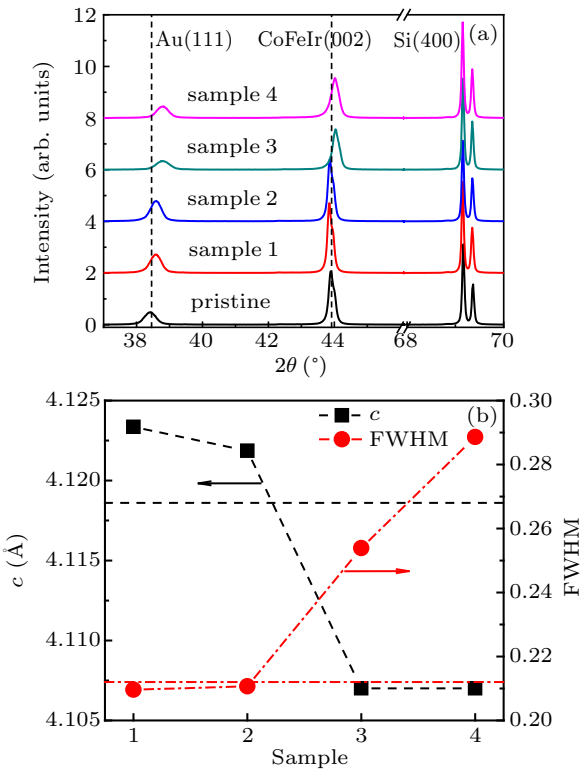


Fig. 2. (a) XRD patterns of the pristine and two groups of hydrogenated samples. (b) c-lattice parameters and FWHM values, determined from the (002) peak of the hcp-$Co_{80}{}^{57}Fe_4Ir_{16}$ phase shown in panel (a). The horizontal dash/dash-dotted line indicates the corresponding value for the pristine sample.

To check the effect of the hydrogenation process on the magnetic properties, as shown in Fig. 3(a), we have made magnetic hysteresis measurements with applied external magnetic field parallel to the film surface. It is clear that both saturation magnetization, M_s, and coercivity, H_c, of the pristine sample have been changed by the hydrogenation process. To see this effect more clearly, the determined M_s and H_c were plotted in Fig. 3(b) with the corresponding values of the pristine sample marked as dash and dash-dotted lines, respectively. We can see that the change of M_s is relatively small and the trend is more or less in a random manner for all these samples, this means that the M_s is less sensitive to the hydrogenation process for the currently studied system. On the other hand, the change of H_c is obviously following the trend of the FWHM values shown in Fig. 2(b). This may be understood with the fact that less disorders were introduced into our films with lower bias voltages and more disorders were introduced with higher bias voltages during the hydrogenation process.

As suggested by our XRD and VSM results, hydrogenation with higher bias voltages might introduce considerable disorders/defects into the crystal structure which have a considerable effect on the coercivity of our films. From our earlier investigations,[29,32] it was known that changes in the coercivity will lead to changes of the high-frequency properties such as the resonance frequency, f_r, and the Gilbert damping constant α, *etc*. Therefore, we present the complex permeability spectra of our pristine and hydrogenated samples together with calculated curves in Figs. 4(a)–4(e). Clearly, the change in the initial permeability is less obvious and following the behavior of the change of M_s in a random manner. On the other hand, the f_r shifts to lower values with increasing disorder. In Fig. 4(f), the extracted f_r and α were plotted with values of the pristine sample marked as horizontal dash and dash–dotted lines, respectively.

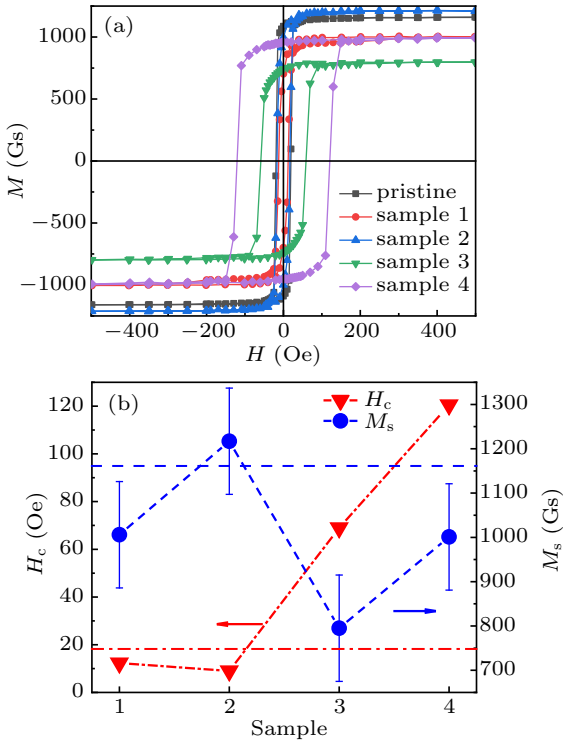


Fig. 3. (a) In-plane magnetic hysteresis loops measured with the applied external magnetic field parallel with the film surface of pristine and hydrogenated samples. (b) The determined coercivity, H_c, and saturation magnetization, M_s, from the hysteresis loops shown in panel (a). The horizontal dash–dotted line and dash line are corresponding values for the pristine sample, respectively. The unit 1 Gs = 10^4 T, 1 Oe = 79.5775 A·m^{-1}.

According to the Landau–Lifshitz–Gilbert (LLG) theory, the measured frequency dependence of the permeability spectra can be described by the following equation:[33,34]

$$\mu = 1 + 4\pi M_s \gamma \frac{\omega_1 + i\alpha\omega}{\omega_1\omega_2 - \omega^2 + i\alpha\omega(\omega_1 + \omega_2)} \quad (1)$$

in which $\omega_1 = \gamma(4\pi M_s - 2K/M_s + H_u) = \gamma(H_\theta + H_u)$, $\omega_2 = \gamma H_u$, where γ is the gyromagnetic ratio, ω is the angular frequency, K is the magnetocrystalline anisotropy constant, $H_\theta = 4\pi M_s - 2K/M_s$ is the total out-of-plane effective magnetic anisotropy field and H_u is the total effective in-plane uniaxial anisotropy field that, in our case, equals to 120 Oe applied externally during the measurements. Then the initial permeability μ_i and resonance frequency f_r can be expressed as[35]

$$\mu_i = 1 + \frac{4\pi M_s}{H_u},$$

$$f_{\rm r} = \frac{\gamma}{2\pi}\sqrt{H_\theta H_{\rm u}}, \tag{2}$$

from which the decreasing $f_{\rm r}$ with increasing disorder can be understood as that the induced disorder results in a decrease of H_θ. Since K is negative for the currently studied system, the decrease in H_θ means a decrease of the absolute value of the magnetocrystalline anisotropy constant $|K|$.

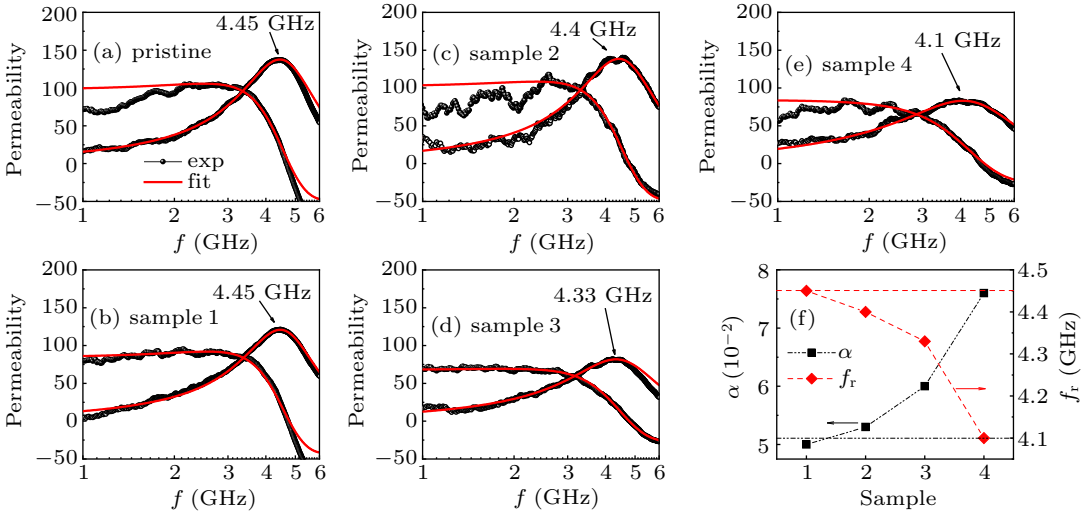


Fig. 4. (a)–(e) Complex permeability spectra (black solid circle and open circle) of the pristine and hydrogenated hcp-$Co_{80}{}^{57}Fe_4Ir_{16}$ films with calculated curves (red line). (f) Resonance frequency $f_{\rm r}$ and Gilbert damping constant α used for calculation of the theoretical curve in panels (a)–(e). The horizontal dash and dash–dotted lines are the corresponding values determined for the pristine sample.

As for the damping constant α, it is well known that it consists two parts, namely, the intrinsic and extrinsic contributions. The first part depends largely on $M_{\rm s}$ and spin–orbit coupling effect,[36] while the second part is generally related to the defect induced two-magnon mode and/or local resonance mode,[37,38] both of which are associated with magnetic inhomogeneities within the material under investigation (*e.g.* anisotropy dispersion and surface or interface roughness). Since the changing behavior of α roughly follows the changing trend of FWHM and $H_{\rm c}$, both of which are highly related to the induced defects in the system, it is safe to say that the extrinsic part plays a decisive role here.

To have a direct overview of the hydrogenation induced defects, we show the measured TEM images and corresponding fast Fourier transform (FFT) diagrams for the pristine sample and hydrogenated samples, sample 1 and sample 4, in Figs. 5(a)–5(c). The identified crystallographic directions were also marked with arrows. It is clear that, the hydrogenated samples exhibit more defects. However, due to the resolution limit of our TEM (especially for magnetic materials), the defect type can not be studied in more detail which should call for further investigations using TEM with atomic resolutions. Nevertheless, a careful check, one can see that the hydrogenated samples exhibit different local regions with different degrees of induced defects. Moreover, from the FFT diagram shown in Fig. 5(c), one can see that the angle between [002] direction and [100] direction clearly deviates from 90° as in contrast for the pristine and sample-1 samples shown in Figs. 5(a)–5(b). This in a clear indication of the defects induced twist of the pristine crystal structure.

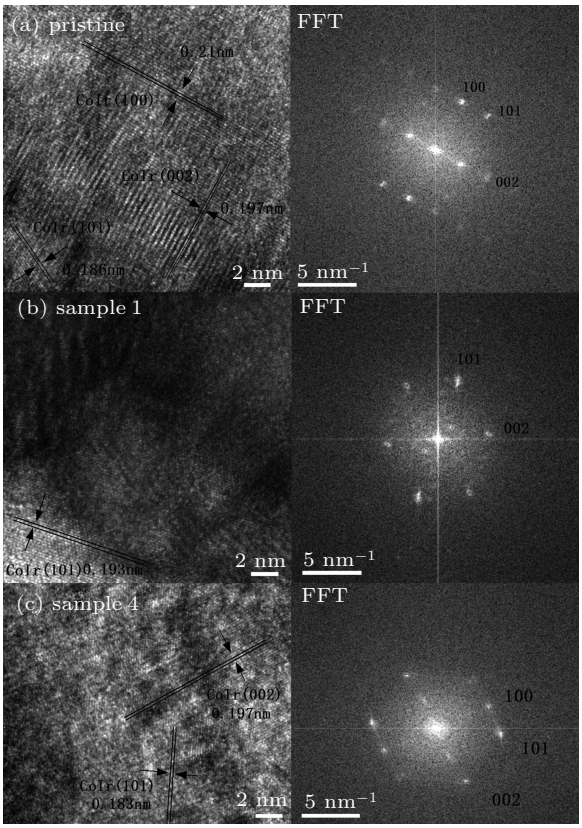


Fig. 5. TEM images with identified crystallograhpic directions marked with arrows and Fourier transform diagrams of the measured samples for (a) pristine sample, (b) hydrogenated sample 1, and (c) hydrogenated sample 4.

To further investigate the local properties, we made CEMS measurements of our films. The left panel of Fig. 6 shows the room temperature CEMS spectra of our pristine and hydrogenated hcp-$Co_{80}{}^{57}Fe_4Ir_{16}$ films measured with the γ-ray traveling perpendicular to the films surface. Similar to

our earlier work, the CEMS spectra of all these films show broad sextets that is typical for metal alloys. This is usually explained as due to the coexistence of different ^{57}Fe sites from the random substitution of the solid solution.[39,40] The spectra were, therefore, fitted with the hyperfine field distribution of a modified version of the Hesse and Rubartsch method by using the Mosswinn programe.[41,42] It is well known that the relative peak intensity of the sextet spectrum is related to the polar angle Θ between the γ-ray and the magnetic moments of the system under study by the following equation:[43]

$$I_{1,6} : I_{2,5} : I_{3,4} = 3(1+\cos^2\Theta) : 4\sin^2\Theta : (1+\cos^2\Theta). \quad (3)$$

Since the thickness of our films studied in this work is only 180 nm, it is reasonable to assume that all the magnetic moments are parallel with the film surface. Thus, the relative peak intensity was fixed to $I_{1,6} : I_{2,5} : I_{3,4} = 3 : 4 : 1$ (means $\Theta = 90°$) in our fitting model. The fitted corresponding distribution of the hyperfine magnetic field was shown in the right panel of Fig. 6. The determined hyperfine parameters from the theoretical fits shown in Fig. 6 were listed in Table 1.

Table 1. Table of the fitted hyperfine parameters for our pristine and hydrogenated hcp-$Co_{80}{}^{57}Fe_4Ir_{16}$ films. Isomer shift δ, quadruple splitting ΔE_Q, average hyperfine magnetic field B_{hf}, and spectral line width Γ_{exp}.

Sample	δ (mm/s)	ΔE_Q (mm/s)	B_{hf} (T)	Γ_{exp} (mm/s)
Pristine	0.03(2)	0.01(4)	24.9(2)	0.30(8)
Sample 1	0.08(2)	0.08(3)	22.3(2)	0.26(8)
Sample 2	0.07(2)	0.00(3)	22.9(2)	0.29(9)
Sample 3	0.07(2)	0.02(3)	22.2(2)	0.28(7)
Sample 4	0.10(2)	0.05(3)	21.3(2)	0.38(8)

From the right panel of Fig. 6, one can see that the major contribution to the hyperfine field is around 26 T for all the measured samples. Another contribution around 20 T, which may be related to the amorphous phases deposited between the grain boundaries and/or from the sample surface part, can also be seen as described in our earlier work.[31] Interestingly, one can see that apart from these two contributions, we found another contribution around 5 T only for the hydrogenated samples. This contribution is absent for the pristine sample and is roughly increasing with the induced defects, and thus is an effect of the hydrogenation process. Another point we would like to address is that the second contribution from the amorphous part of the sample has also been enhanced by the hydrogenation process.

These results suggest that the hydrogenation process may have two different effects. The first one is that at low bias voltages the process is less destructive and the implanted hydrogen stays mainly at the interstitial sites and/or the amorphous phases[20] which expands the crystal structure as observed by our XRD measurements for the group-1 samples. The second one is that at higher bias voltages the energy of the implanted hydrogen is high enough to make more destructive effects to the crystal structure which is similar to the high energy hydrogen irradiation process.[44,45] This process happens most likely at the Ir site due to its much bigger atomic size and thus higher probability to interact with the injected protons. This process may cause segregation of a small portion of the Ir content at small regions such as the interface and/or the surface of the film, which is still below the detection limit of our XRD. But, a small deviation of the Ir content for the main phase is already enough to induce an observable shift of the (002) peak as shown in Fig. 2. This is further corroborated by the rightwards shift of the (111) peak of the Au seed layer for all samples since it has a similarly large atomic size with Ir. We would like to note that from our CEMS measurements, right panel of Fig. 6, both defects exist for low and high bias voltage protonations. Together with our XRD results, we may conclude that the non-destructive defects are the dominant defects for the low bias voltage case and the destructive defects are the main defects for the high voltage case.

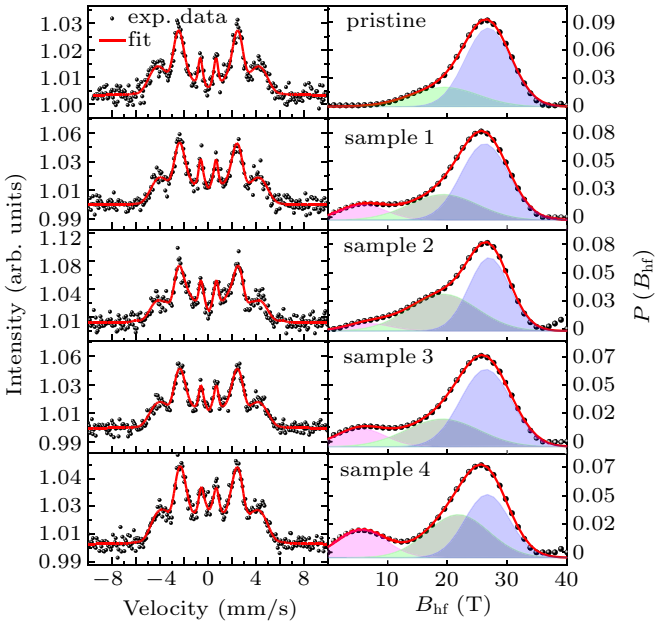


Fig. 6. Left panel presents the measured CEMS spectra (black dots) with the γ-ray perpendicular to the film plane for our pristine and hydrogenated hcp-$Co_{80}{}^{57}Fe_4Ir_{16}$ films. The red solid lines through the data points are theoretical fits as described in the text. Right panel shows the corresponding field distribution of the theoretical fits with different contributions (see text).

As for the magnetic properties, these induced defects may act as pining centers which will affect the movement of the domain walls during magnetization reversal. Kersten *et al*. proposed a strong pinning model of defect at low domain wall energy,[46] In this model, the domain wall will bend under the applied external magnetic field to counteract the force exerted on the domain wall with the following relation:

$$\frac{E}{r} = 2\mu_0 M_s H\cos\theta, \quad (4)$$

where E is the domain wall energy, H is the external magnetic field, r is the radius of the curvature of the wall, and θ is the angle between H and the domain wall. The coercive force can then be described as

$$H_c = \frac{E}{\mu_0 M_s l \cos\theta}, \tag{5}$$

where l is the distance between different pinning positions. This means that the coercive force of the magnetic material is directly proportional to the defect density. Then, the increase of the coercive force shown in Fig. 3 can be understood naturally.

4. Conclusion

In conclusion, two groups of hydrogenated samples, acquired by using low and high energy protons, of the hcp-$Co_{80}{}^{57}Fe_4Ir_{16}$ soft magnetic thin films have been studied. Our results show that the hydrogen ions accumulate mainly at the interfacial regions and/or the amorphous phases in our sample for the non-destructive low energy case. On the other hand, for the high energy destructive case, the crystal structure was damaged and segregation of elements with bigger atomic size may appear. The magnetic properties such as the coercivity, resonance frequency, magnetocrystalline anisotropy constant K, and magnetic damping constant α can be greatly tuned by the density of the induced defects. Therefore, these results provide a new way for materials processing and a new platform to study the interplay between different defects and the properties of the materials.

References

[1] Lou J, Reed D, Liu M and Sun N X 2009 *Appl. Phys. Lett.* **94** 112508
[2] Liu G X, Cui X X and Dong S X 2010 *J. Appl. Phys.* **108** 094106
[3] Zhang H W, Liu Y L and Zhong Z Y 2001 *Vacuum* **62** 1
[4] Phuoc N N, Xu F and Ong C K 2009 *Appl. Phys. Lett.* **94** 092505
[5] Yamaguchi M, Miyazawa Y, Kaminishi K, Kikuchi H, Yabukami S, Arai K I and Suzuki T 2004 *J. Magn. Magn. Mater.* **268** 170
[6] Feng E, Wang Z K, Du H M, Wei J W, Cao D R, Liu Q F and Wang J B 2014 *J. Appl. Phys.* **115** 17A307
[7] Wang W, Chen Y, Yue G H, Sumiyama K, Hihara T and Peng D L 2009 *J. Appl. Phys.* **106** 013912
[8] Guo X B, Xi L, Li Y, Han X M, Li D, Wang Z and Zuo Y L 2014 *Appl. Phys. Lett.* **105** 072411
[9] Liu S Y, Ma Y H, Chang L, Li G J, Wang J H and Wang Q 2018 *Thin Solid Films* **651** 1
[10] Yao D S, Zhou X Y, Zuo H P and Zhang B M 2008 *Appl. Surf. Sci.* **254** 2556
[11] Liu S H, Hsiao S N, Chen S K and Lee H Y 2015 *J. Alloys Compd.* **631** 15
[12] Mallik S, Mallick S and Bedanta S 2017 *J. Magn. Magn. Mater.* **428** 50
[13] Singh A K and Alagarsamy P 2016 *J. Magn. Magn. Mater.* **401** 1015
[14] Chotibhawaris T, Luangvaranunt T, Jantaratana P and Boonyongmaneerat Y 2018 *Intermetallics* **93** 323
[15] Singh A K and Hsu J H 2017 *J. Magn. Magn. Mater.* **432** 96
[16] Ma T Y, Jiao J Y, Li Z W, Qiao L, Wang T and Li F S 2017 *J. Magn. Magn. Mater.* **444** 119
[17] Yoon H, Choi M, Lim T W, Kwon H, Ihm K, Kim J K, Choi S Y and Son J 2016 *Nat. Mater.* **15** 1113
[18] Jo M, Lee H J, Oh C, Yoon H, Jo J Y and Son J 2018 *Adv. Funct. Mater.* **28** 1802003
[19] Hope M A, Griffit K J, Cui B, Gao F, Dutton S E, Parkin S S P and Grey C P 2018 *J. Am. Chem. Soc.* **140** 16685
[20] Wu M, Chen S Q, Huang C W, Ye X, Zhou H P, Huang X C, Zhang K H L, Yan W S, Zhang L H, Kim K, Du Y, Chembers S, Zheng J C and Wang H Q 2020 *Front. Phys.* **15** 13601
[21] Smith K A, Savva A I, Deng C J, Wharry J P, Hwang S, Su D, Wang Y Q, Gong J, Xu T, Butt D P and Xiong H 2017 *J. Mater. Chem. A* **5** 11815
[22] Lu N P, Zhang P F, Zhang Q H, *et al.* 2017 *Nature* **546** 124
[23] Ho K Y, Chen W Z and Gui R L 1990 *IEEE Trans. Magn.* **26** 1424
[24] Zamani A, Hallen A, Nordblad P, Andersson G, Hjorvarsson B and Jonsson P E 2013 *J. Magn. Magn. Mater.* **346** 138
[25] Pourarian F, Wallace W E and Malik S K 1982 *J. Less-Common Met.* **83** 95
[26] Trinkaus T, Hollander B, Rongen S, Mantl S, Herzog H J, Kuchenbecker J and Hackbarth T 2000 *Appl. Phys. Lett.* **76** 3552
[27] Barcz A, Kozubal M, Jakieła R, Ratajczak J, Dyczewski J, Gołaszewska K, Wojciechowski T and Celler G K 2014 *J. Appl. Phys.* **115** 223710
[28] Tong Q Y, Gutjahr K, Hopfe S, Gösele U and Lee T H 1997 *Appl. Phys. Lett.* **70** 1390
[29] Ma T Y, Jiao J Y, Li Z W, Qiao L, Wang T and Li F S 2018 *Appl. Surf. Sci.* **457** 598
[30] Zhang S, Xu F, Ma X M, Wang T, Tan G G and Li F S 2014 *Appl. Surf. Sci.* **299** 81
[31] Luo Z, Ma T Y, Li Y, Li Z W, Wang T and Li F S 2019 *J. Supercond. Nov. Magn.* **32** 3957
[32] Ma T Y, Luo Z, Li Z W, Qiao L, Wang T and Li F S 2019 *Chin. Phys. B* **28** 057505
[33] Phuoc N N, Xu F and Ong C K 2009 *J. Appl. Phys.* **105** 113926
[34] Ge S H, Yao D S, Yamaguchi M, Yang X L, Zuo H P, Ishii T, Zhou D and Li F S 2007 *J. Phys. D: Appl. Phys.* **40** 3660
[35] Xue D S, Li F S, Fan X L and Wen F S 2008 *Chin. Phys. Lett.* **25** 4120
[36] Kambershy V 1970 *Can. J. Phys.* **48** 2906
[37] Arias R and Mills D L 1999 *Phys. Rev. B* **60** 7395
[38] Chappert C, Dang K L, Beauvillain P, Hurdequint H and Renard D 1986 *Phys. Rev. B* **34** 3192
[39] Oliveira L S, Cunha J B M, Spada E R and Hallouche B 2007 *Appl. Surf. Sci.* **254** 347
[40] Cohen N S, Pankhurst Q A and Barquin L F 1999 *J. Phys.: Condens. Matter* **11** 8839
[41] Hesse J and Rubartsch A 1974 *J. Phys. E: Sci. Instrum.* **7** 526
[42] Klencsar Z, Kuzmann E and Vertes A 1996 *J. Radioanal. Nucl. Chem.* **210** 105
[43] Preston R S, Hanna S S and Heberle J 1962 *Phys. Rev.* **128** 2207
[44] Wang L M, Wang S X, Ewing R C, Meldrum A, Birtcher R C, Provencio P N, Weber W J and Matzke H 2000 *Mater. Sci. Eng. A* **286** 72
[45] Jiao Z and Was G S 2011 *Acta Mater.* **59** 1220
[46] Kersten M 1956 *Z. Angew. Phys.* **8** 496